J Mater Sci: Mater Electron (2017) 28:11569–11575
DOI 10.1007/s10854-017-6957-8

Preparation of yolk–shell Fe_3O_4@N-doped carbon nanocomposite particles as anode in lithium ion batteries

Ting-Ting Yang[1] · Wen-Kai Zhu[1] · Wei-Liang Liu[1] · Fan-Gong Kong[2] · Man-Man Ren[1] · Qin-Ze Liu[1] · Zhi-Zhou Yang[1] · Xin-Qiang Wang[3] · Xiu-Lan Duan[3]

Received: 21 February 2017 / Accepted: 13 April 2017 / Published online: 24 April 2017

Abstract The yolk–shell-structured Fe_3O_4 nanocomposite particles (Fe_3O_4@Void@C–N NPs) with Fe_3O_4 as the yolk and N-doped carbon as the shell were prepared by using melamine formaldehyde resin as the N and C sources. When used as anode material for lithium ion battery, the yolk–shell structure could not only afford adequate void to accommodate the large volume change during charge/discharge process but also improve structural stability and electrical conductivity. The anode material demonstrated superior long-term and high-rate performance because of the novel structure and the N-doped carbon shell with mesopore. Thus, Fe_3O_4@Void@C–N NPs exhibited a high reversible capacity of 1530 mAh g^{-1} after 300 cycles at a current density of 500 mA g^{-1}, which were approximately 1.5 and 6 times higher than Fe_3O_4@C–N NPs and pure Fe_3O_4 particles, respectively. Even at the higher current density of 2000 mA g^{-1}, the reversible capacity remained at 651 mAh g^{-1} after 500 cycles.

Electronic supplementary material The online version of this article (doi:10.1007/s10854-017-6957-8) contains supplementary material, which is available to authorized users.

✉ Wei-Liang Liu
wlliu@sdu.edu.cn

✉ Fan-Gong Kong
kfg@qlu.edu.cn

[1] School of Materials Science and Engineering, Qilu University of Technology, Daxue Road, Western University Science Park, Jinan 250353, People's Republic of China

[2] Key Laboratory of Pulp and Paper Science and Technology of Ministry of Education/Shandong Province of China, Qilu University of Technology, Jinan 250353, China

[3] State Key Laboratory of Crystal Materials, Shandong University, Jinan 250100, People's Republic of China

1 Introduction

Lithium ion batteries (LIBs) have attracted considerable attention in both scientific and industrial fields due to their high energy density. The next generation of LIBs is expected to have superior performances in terms of capacity, cycling stability, and rate capability to meet the requirements of new emerging technologies. This goal significantly relies on developing a new generation of anode materials, which plays a crucial role in the performance of LIBs.

Commercial graphite has a relatively low theoretical capacity of 372 mAh g^{-1} [1], which has limited its application as an anode material. Various novel anode materials have been proposed previously to replace traditional anodes. Among these alternatives, transition metal oxides (TMOs), such as iron oxides [2–5], cobalt oxides [6, 7] and nickel oxides [8, 9], are considered as promising anode materials for LIBs because of their high theoretical capacities, which is commonly several times higher than that of graphite. Particularly, ferroferric oxide (Fe_3O_4) has shown great potential because of its special features, such as high theoretical specific capacity (926 mAh g^{-1}), low cost, natural abundance, and eco-friendliness [10–12]. Nevertheless, the commercial application of Fe_3O_4 was hindered by poor rate and cycling performance due to the severe volume expansion upon lithiation, which is common for TMOs [13, 14].

Accordingly, various strategies were proposed to overcome the abovementioned drawbacks of Fe_3O_4. Two effective methods involve the design of unique nanostructures, such as nanotubes [15], hollow nanospheres [16, 17], and nanorods [18, 19], and the composition with carbonaceous materials, which can shorten the diffusion length for lithium ion, thereby avoiding direct contact with electrolytes

and effectively accommodating the mechanical strain. Several previous reports have shown that adopting the combination of the two methods is suitable to improve the electrochemical performance of Fe_3O_4 markedly, avoiding the aggregation and constant consumption of nanomaterials [20–22].

Nitrogen-doped carbon has been reported to demonstrate increased electrical conductivity and Li-storage capacity [23, 24]. The introduction of nitrogen offers favorable and active sites for lithium ion, which is remarkably beneficial in achieving the charge–discharge cycle [25]. A uniform distribution of nitrogen in the carbon crystal lattice can improve the electrochemical performance.

In our work, melamine formaldehyde (MF) resin was used as particular N and C sources to prepare yolk–shell-structured active materials. The electrochemical performance of yolk–shell-structured Fe_3O_4 nanocomposite particles (Fe_3O_4@Void@C–N NPs) was studied and showed a high reversible capacity of 1530 and 651 mAh g^{-1} after 300 and 500 cycles at a current density of 500 and 2000 mA g^{-1}, respectively. This study might enlighten the search for preferable strategies in developing advanced anode materials for LIBs or other energy storage devices.

2 Experimental

2.1 Materials synthesis

The procedures for the synthesis of Fe_3O_4@Void@C–N NPs are shown in Scheme 1. All chemicals were analytical grade and used without further purification. The uniform Fe_3O_4 particles were prepared according to the published procedure described in the literature [26]. Fe_3O_4@SiO_2 NPs were synthesized by the modified Stöber method [27]. The MF shell was prepared using glacial acetic acid catalyzed referencing the MF sphere procedure [28]. Finally, the Fe_3O_4@Void@C–N NPs were obtained by calcining the Fe_3O_4@SiO_2@MF NPs in tube furnace and etching with NaOH. The details were described in supporting information. The Fe_3O_4@C–N NPs were prepared under the same conditions except the synthesis of SiO_2 layer and the subsequent etch treatment.

2.2 Characterization

The morphologies and microstructures were investigated using a JEM-100CX II transmission electron microscope (TEM) at an accelerating voltage of 200 kV. X-ray diffraction (XRD) patterns obtained on a D/Max-RB X-ray diffractometer (Bruker AXS, Germany) with Cu Kα irradiation at a scanning range of 10°–70° were used to determine the phase structures of the samples. Fourier transform infrared (FTIR) spectra of the samples were recorded using a Nicolet iS10 FTIR spectrometer. Thermogravimetric analysis (TGA) was carried out on TGA 1 SF/1100 (METTLER TOLEDO), under air flow with heating rate of 10 °C/min. The surface area and pore size were estimated by Brunauer–Emmett–Teller (BET) and Barrett–Joyner–Halenda (BJH) methods, respectively. Magnetic characterization was performed on a Quantum Design MPMS XL-7 super-conducting quantum interference magnetometer.

2.3 Electrochemical measurements

Electrochemical experiments were performed with 2032 coin-type cells, with lithium metal as the counter and reference electrode and a solution of 1 M $LiPF_6$ dissolved in a 1:1:1 mixture solution of ethylene carbonate, dimethyl carbonate, and ethylene methyl carbonate as electrolyte, and assembled in an Ar-filled glove box. The working electrodes were fabricated by casting a slurry of active material, acetylene black, and polyvinylidene fluoride (70:20:10 in weight ratio) in *N*-methylpyrrolidinone solvent onto pure copper foil. The as-prepared electrodes were dried at 100 °C for 10 h in vacuum, and then cut into circular pieces of about 12 mm in diameter. Each cell was aged for 12 h at room temperature before commencing the electrochemical tests. Galvanostatic charge/discharge tests were performed on a LAHE battery test system at various current densities in the potential range of 0.01–3.00 V (vs. Li/

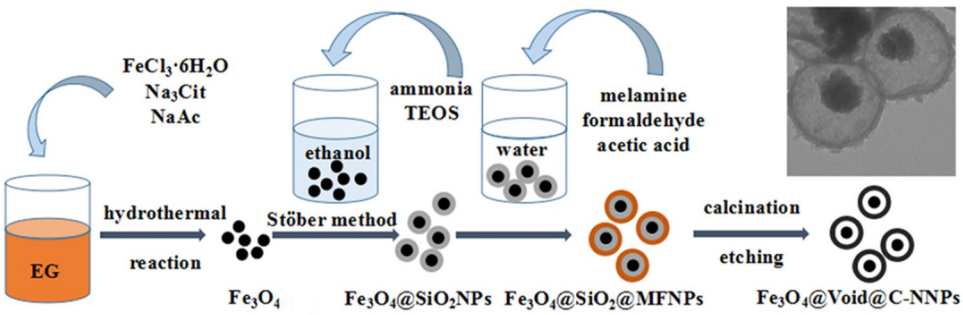

Scheme 1 Schematic illustration of the synthesis procedures of Fe_3O_4@Void@C–N NPs

Li^+) at room temperature. Cyclic voltammograms (CV) and electrochemical impedance spectroscopy (EIS) were conducted on a CHI660E electrochemical workstation. The CV curves were recorded in 0.01–3.00 V at a scanning rate of 0.05 mV/s. EIS was tested at the frequency ranging from 10 kHz to 0.01 Hz with an AC signal of 5 mV in amplitude as the perturbation.

3 Results and discussion

3.1 Structure characterization

The size and morphology of the obtained particles were examined by TEM (Fig. 1). Figure 1a shows that the pure Fe_3O_4 particles with a diameter ~200 nm are rough and nearly monodispersed. SiO_2 was used as a sacrificial layer to cover Fe_3O_4 particles, and the thickness is ~100 nm (Fig. 1b). As shown in Fig. 1c, d, the thickness of N-doped carbon shell is approximately 10 nm.

Figure 2a shows the XRD patterns of the synthesized Fe_3O_4@Void@C–N NPs, and all the peaks could be indexed to magnetite Fe_3O_4 (JCPDS card 75-0033). Compared with that of pure Fe_3O_4, the decrease and increase in intensity of Fe_3O_4 diffraction demonstrate the success of coating and etching. Moreover, the additional broad diffraction peak at 22.09° could be assigned to the characteristic peak of the disorderedly stacked amorphous carbon.

The particles were characterized by FTIR spectra (Fig. 2b) to confirm MF formation. The peak 583 cm^{-1} could be assigned to Fe–O vibration, whereas the one at 1635 cm^{-1} could be assigned to the stretching vibration of the carbonyl group on the Fe_3O_4 surface. As a result of SiO_2 coating, the peaks were detected at 1095, 799 and 958 cm^{-1}, which are associated with the asymmetric and symmetric stretching vibrations of Si–O–Si and the vibration of Si–O–H. The peaks at 1560 and 814 cm^{-1} are attributed to the 1,3,5-s-triazine ring [29]. The disappearance of the characteristic peak of SiO_2 indicates void formation.

The TGA of Fe_3O_4@Void@C–N and Fe_3O_4@C–N NPs were performed in air from 45 to 1000 °C at a rate of 10 °C/min to quantify the amount of N-doped carbon (Fig. S1). The weight ratios of the N-doped carbon layers of Fe_3O_4@C–N and Fe_3O_4@Void@C–N NPs were

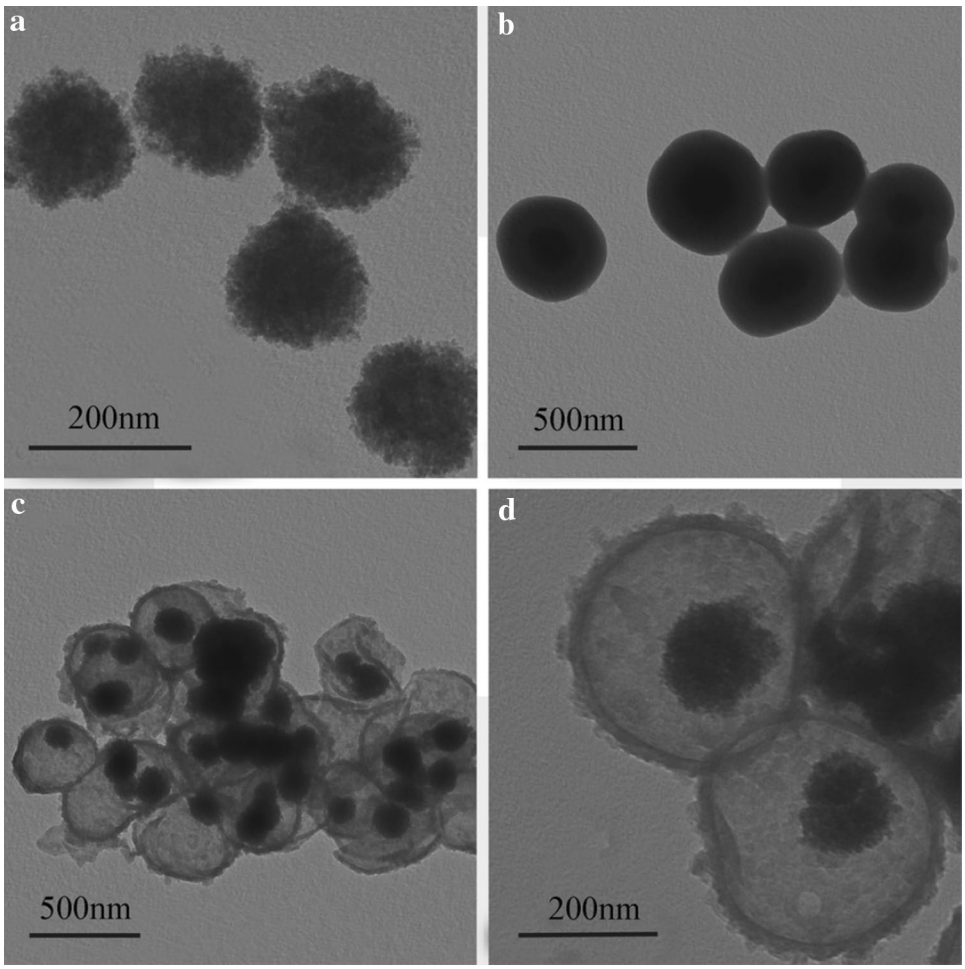

Fig. 1 TEM images of **a** Fe_3O_4, **b** Fe_3O_4@SiO_2 NPs, **c** Fe_3O_4@Void@C–N NPs, and **d** Fe_3O_4@Void@C–N NPs at higher magnification

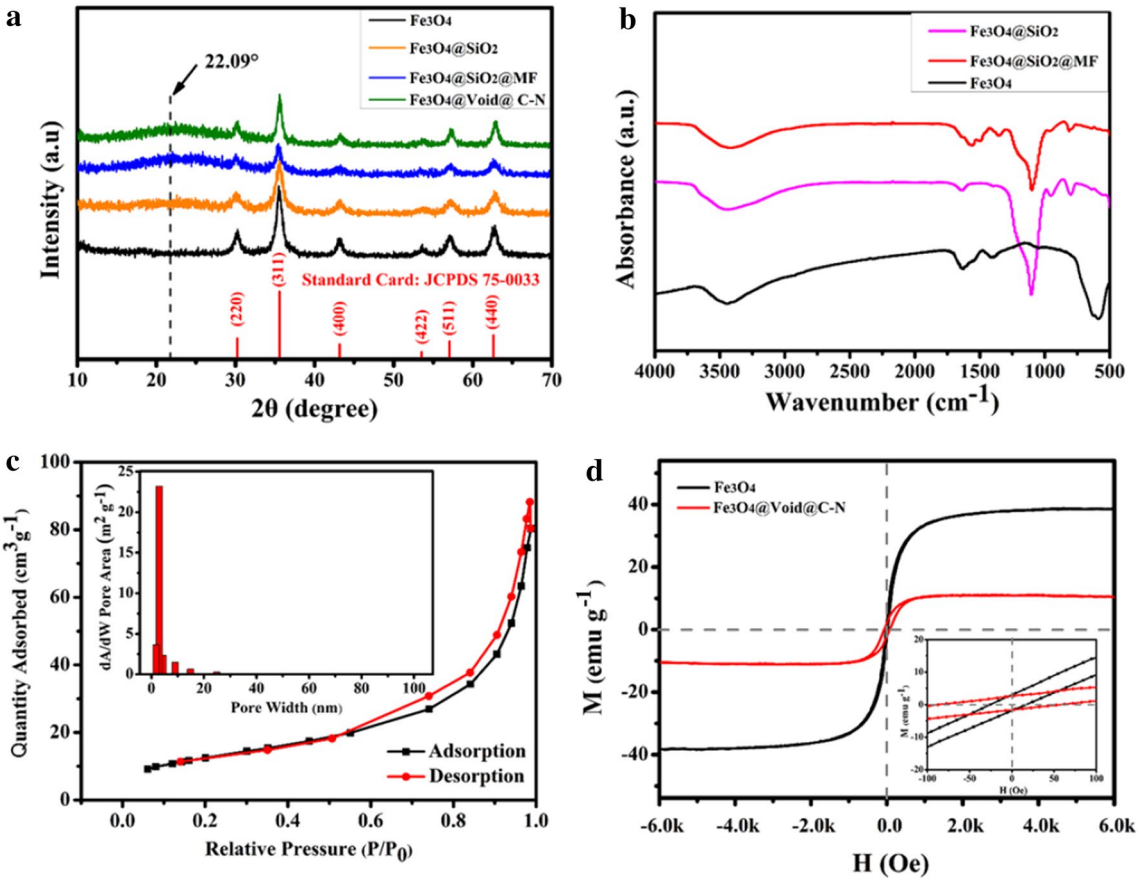

Fig. 2 **a** XRD patterns and **b** FTIR spectra of Fe_3O_4, Fe_3O_4@SiO_2, Fe_3O_4@SiO_2@MF and Fe_3O_4@Void@C–N NPs; **c** N_2 adsorption desorption isotherm and pore size distribution curve (*inset*); **d** The hysteresis loops and the magnified low field curve (*inset*) of Fe_3O_4 and Fe_3O_4@Void@C–N NPs

approximately 11.33 and 3.33%, respectively. Nitrogen adsorption–desorption isotherms were adopted to characterize the BET specific surface area and porous structure of the as-prepared Fe_3O_4@Void@C–N NPs (Fig. 2c). The BET specific surface area of Fe_3O_4@Void@C–N NPs is 45.84 $m^2\ g^{-1}$, which is higher than the reported value for the pure Fe_3O_4 (11 $m^2\ g^{-1}$) [30]. Moreover, the pore size is ~3.0 nm based on the BJH model, suggesting the existence of mesopore in the shell performance (inset of Fig. 2c). The large surface area and porous structure not only allow adequately contact between active materials and electrolyte but also facilitate the improvement of the electrochemical performance. Magnetic characterization was also conducted by a vibrating sample magnetometer at room temperature. As shown in Fig. 2d, the saturation magnetization values (Ms) of Fe_3O_4 and Fe_3O_4@Void@C–N NPs were measured to be 11.06 and 39.14 emu g^{-1}, respectively. Notably, the coercivity (Hc) value for Fe_3O_4 particles was 25.5 Oe (inset of Fig. 2d), which was less than the theoretical value for superparamagnetic particles (Hc ≤ 50 Oe) [31].

3.2 Electrochemical properties

Electrochemical performance was investigated by galvanostatic discharge–charge and CV measurements. Fig. S2 and Fig. 3a showed the discharge–charge curves of pure Fe_3O_4, Fe_3O_4@C–N and Fe_3O_4@Void@C–N electrodes at a current density of 100 mA g^{-1}. As shown in Fig. 3a, the initial discharge curve demonstrates a long voltage plateau at approximately 0.8 V, which corresponds to the reduction of Fe_3O_4 to Fe^0 [32] and the insertion of Li ion into the electrode. After the 2nd cycle the charge/discharge curves almost overlapped, reflecting the excellent cycle stability of Fe_3O_4@Void@C–N NPs. The initial discharge capacity of Fe_3O_4@Void@C–N NPs was 2276 mAh g^{-1}, whereas the reversible discharge capacities remained at 1569, 1518, 1472, and 1461 mAh g^{-1} after 2, 3, 5, and 10 cycles, respectively. The loss may result from the incomplete conversion reaction and irreversible lithium loss due to the formation of solid electrolyte interface (SEI) layer [33]. In the case of Fe_3O_4 and Fe_3O_4@C–N NPs, the discharge capacities decreased to 371 and 515 mAh g^{-1}

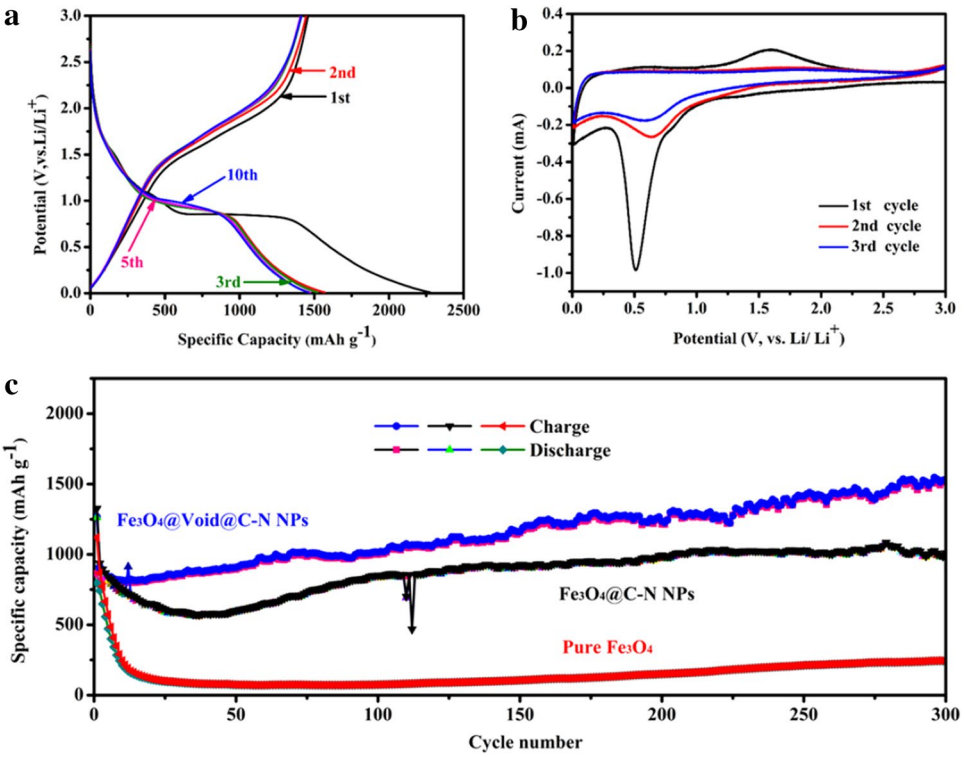

Fig. 3 **a** The discharge–charge curves of Fe_3O_4@Void@C–N NPs in the potential range of 0.01 and 3.0 V (vs. Li/Li^+) at a current density of 100 mA g^{-1}; **b** cyclic voltammetry curves of Fe_3O_4@Void@C–N NPs in the potential range of 0.01 and 3.0 V (vs. Li/Li^+) at a scan rate of 0.05 mV/s; **c** cycling performance of pure Fe3O4, Fe_3O_4@C–N NPs and Fe_3O_4@Void@C–N NPs at the current density of 500 mA g^{-1}

after 10 cycles, respectively (Fig. S2). Figure 3b presents the CV profile of Fe_3O_4@Void@C–N NPs for the initial three cycles. In the 1st cathodic process, an obvious peak at 0.5 V was found, which was usually ascribed to the reduction of Fe_3O_4 to Fe^0 in the conversion reaction $Fe_3O_4 + 8e^- + 8Li^+ \rightarrow Fe^0 + 4Li_2O$ and the formation of SEI layer [34–36]. In the 1st anodic process, the peak at ~1.6 V could be observed, corresponding to the electrochemical oxidation of reactions ($Fe^0 \rightarrow Fe^{2+}$, Fe^{3+}). In the 2nd and 3rd cycles, the cathodic peaks shifted to 0.6 V, and the curves nearly overlapped indicating proper reversibility during cycling, which conforms to the discharge–charge curves.

The cycling and high-rate performance of the Fe_3O_4@Void@C–N NPs electrode were also evaluated by the extended discharge/charge experiments. Figure 3c presents the cycling performance of Fe_3O_4@Void@C–N electrode at the current density of 500 mA g^{-1}. For Fe_3O_4@Void@C–N NPs, the specific discharge capacity initially decreased to a minimum of 812 mAh g^{-1} at the 11th cycle, which gradually increased and finally stabilized at 1530 mAh g^{-1} at the 300th cycle. By contrast, the specific discharge capacity of pure Fe_3O_4 decayed to 242 mAh g^{-1}, and Fe_3O_4@C–N NPs maintained at 1005 mAh g^{-1} after 300 cycles. The capacity rise may be ascribed to the additional capacity storage of the N-doped carbon shell at the low potential and the activation of the active materials over the following cycles [34, 37]. In addition, the specific capacities of Fe_3O_4@C–N and Fe_3O_4@Void@C–N NPs were higher than the theoretical specific capacities, 863 and 908 mAh g^{-1}, which were calculated according to TGA. This result may be ascribed to the existence of activation and stabilization for anode materials, which is similar to other reported metal oxides [38–40]. Fe_3O_4@Void@C–N NPs exhibited excellent long-term cycling stability at a higher current density of 2000 mA g^{-1} due to the large void and N-doped carbon shell (Fig. 4a). A favorable capacity of 651 mAh g^{-1} could be retained after 500 cycles with a columbic efficiency of ~100%.

Table S1 lists and compares the structure and high-rate performance of Fe_3O_4@Void@C–N NPs in this study and other Fe_3O_4 anodes reported in literature. The Fe_3O_4@Void@C–N electrode presents remarkably better high-rate performances than those previously reported [22].

Figure 4b presents the rate performance of Fe_3O_4@Void@C–N NPs electrode at various current rates from 200 to 1000 mA g^{-1}. High capacity of 365 mAh g^{-1} was delivered at 1000 mA g^{-1}. When the current densities switched back from 1000 to 200 mA g^{-1}, the capacity could be recovered perfectly, demonstrating the excellent rate performance resulting from the special yolk–shell structure, which contained uniform N-doped carbon shell and void. Figure 5 presents the typical Nyquist plots obtained for pure Fe_3O_4, Fe_3O_4@C–N and Fe_3O_4@Void@C–N electrodes during the initial cycles. A semicircle appeared in the high-frequency region [41, 42] followed by a straight

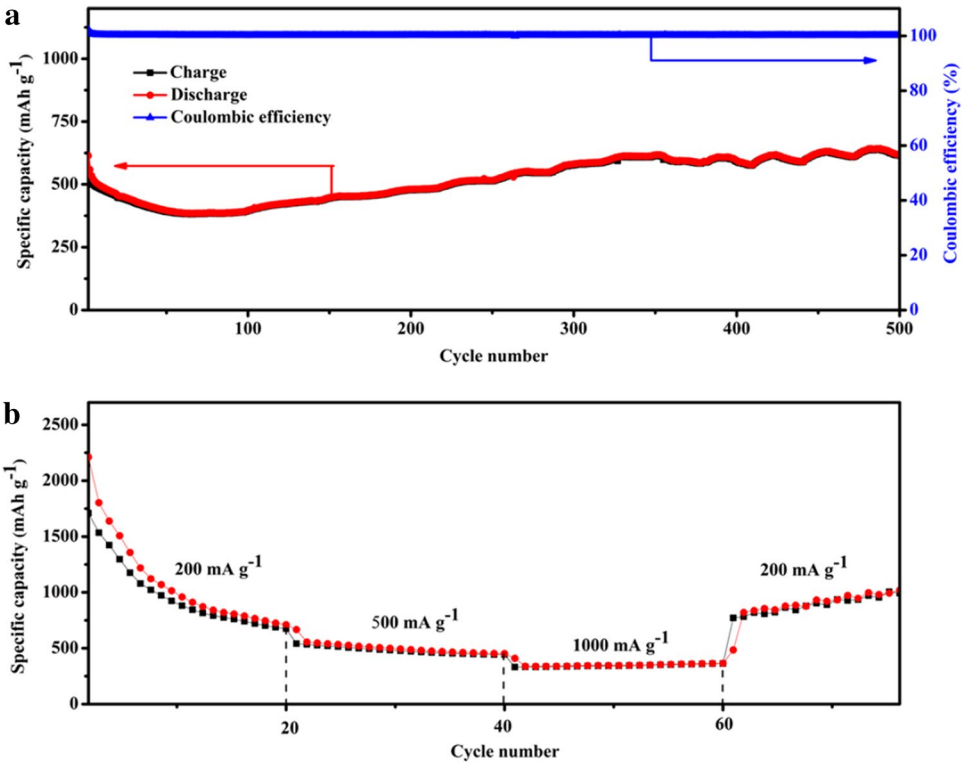

Fig. 4 **a** Long-term cycling test of Fe_3O_4@Void@C–N NPs at the current density of 2000 mA g^{-1}; **b** rate capability of Fe_3O_4@Void@C–N NPs electrode at current rates from 200 to 1000 mA g^{-1} for 20 cycles

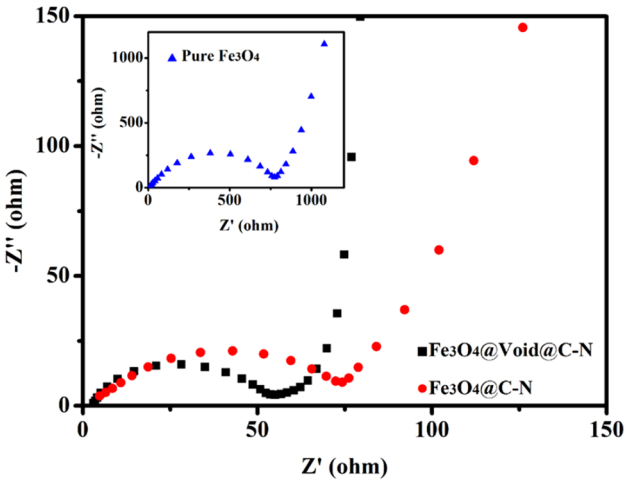

Fig. 5 Nyquist plots of Fe_3O_4@C–N, Fe_3O_4@Void@C–N NPs and pure Fe_3O_4 (*inset*) electrodes during the initial cycles

line in the low-frequency region [43, 44]. The radius of the semicircle was related to the charge transfer resistance (Rct) in the electrode/electrolyte interface [45]. The slope of the straight lines reflected the diffusion coefficients of lithium ion in samples. Evidently, the diameter of the semicircle for Fe_3O_4@Void@C–N NPs was significantly smaller than that of the other two electrodes, suggesting a smaller Rct. Furthermore, the steeper inclined line of Fe_3O_4@Void@C–N NPs manifested faster Li ion diffusion. The results further verified the benefits of yolk–shell structure and the N-doped carbon shell of Fe_3O_4@Void@C–N NPs in enhancing the electrochemical properties of electrodes.

4 Conclusion

In summary, the yolk–shell-structured Fe_3O_4@Void@C–N NPs were successfully designed and fabricated. The void could offer adequate space to buffer the large volume change of Fe_3O_4 during charge/discharge process. Introducing of MF as the precursor of N-doped carbon shell with mesoporous structure avoided the aggregation of Fe_3O_4 particles and efficiently improved the electrochemical performance. Thus, electrochemical tests demonstrated that the lithium storage performances of Fe_3O_4@Void@C–N NPs were higher than pure Fe_3O_4 and Fe_3O_4@C–N electrodes. This study could help in fabricating useful metal oxides in other energy storage fields.

Acknowledgements The work described in this paper was supported by Shandong Province Natural Science Foundation (ZR2012EMM009 and ZR2013EMQ005), the Scientific Research Foundation for the Returned Overseas Scholars in Jinan (20100406), National Natural Science Foundations of China (51372140, 31570566, 31500489, 51503107 and 51172130), and the Foundation of Key Laboratory of Pulp and Paper Science and Technology of Ministry of Education/Shandong Province of China (No. KF201602).

References

1. E.M.J. Li, J. Winnick, P.A. Kohl, J. Power Sources **102**, 294–301 (2001)
2. X. Lou, J. Huang, T. Li, H. Hu, Y. Zhang, J. Mater. Sci. Mater. Electron. **25**, 1193–1196 (2014)
3. Y. Dong, K.C. Yung, R. Ma, X. Yang, Y.-S. Chui, J.-M. Lee, J.A. Zapien, Carbon **86**, 310–317 (2015)
4. J.S. Chen, Y. Zhang, X.W. Lou, ACS Appl. Mater. **3**, 3276–3279 (2011)
5. X. Wang, Y. Liu, H. Arandiyan, H. Yang, L. Bai, J. Mujtaba, Q. Wang, S. Liu, H. Sun, Appl. Surf. Sci. **389**, 240–246 (2016)
6. Z.-S. Wu, W. Ren, L. Wen, L. Gao, J. Zhao, Z. Chen, G. Zhou, F. Li, H.-M. Cheng, ACS Nano **4**, 3187–3194 (2010)
7. D. Bresser, E. Paillard, P. Niehoff, S. Krueger, F. Mueller, M. Winter, S. Passerini, Chem. Phys. Chem. **15**, 2177–2185 (2014)
8. B. Wang, G. Wang, X. Cheng, H. Wang, Chem. Eng. J. **306**, 1193–1202 (2016)
9. L. Gu, W. Xie, S. Bai, B. Liu, S. Xue, Q. Li, D. He, Appl. Surf. Sci. **368**, 298–302 (2016)
10. P.L. Taberna, S. Mitra, P. Poizot, P. Simon, J.M. Tarascon, Nat. Mater. **5**, 567–573 (2006)
11. B. Wang, H.B. Wu, L. Zhang, X.W. Lou, Angew. Chem. Int. Ed. **52**, 4165–4168 (2013).
12. W. Wei, S. Yang, H. Zhou, I. Lieberwirth, X. Feng, K. Muellen, Adv. Mater. **25**, 2909–2914 (2013)
13. C. Zhang, Z. Chen, Z. Guo, X.W. Lou, Energy Environ. Sci. **6**, 974–978 (2013)
14. Y. Wang, Y. Wang, D. Jia, Z. Peng, Y. Xia, G. Zheng, Nano Lett. **14**, 1080–1084 (2014)
15. H. Cao, R. Liang, D. Qian, J. Shao, M. Qu, J. Phys. Chem. C **115**, 24688–24695 (2011)
16. M. Sasidharan, N. Gunawardhana, M. Yoshio, K. Nakashima, Ionics **19**, 25–31 (2013)
17. H. Geng, Q. Zhou, J. Zheng, H. Gu, RSC Adv. **4**, 6430–6434 (2014)
18. A. Hu, X. Chen, Q. Tang, B. Zeng, Ceram. Int. **40**, 14713–14725 (2014)
19. J. Jiao, W. Qiu, J. Tang, L. Chen, L. Jing, Nano Res. **9**, 1256–1266 (2016)
20. C. Wang, G. Shao, Z. Ma, S. Liu, W. Song, J. Song, Electrochim. Acta **130**, 679–688 (2014)
21. J. Zhao, S. Zhang, W. Liu, Z. Du, H. Fang, Electrochim. Acta **121**, 428–433 (2014)
22. L. Yang, G. Guo, H. Sun, X. Shen, J. Hu, A. Dong, D. Yang, Electrochim. Acta **190**, 797–803 (2016)
23. M. Li, J. Xue, J. Phys. Chem. C **118**, 2507–2517 (2014)
24. W. Ai, J. Jiang, J. Zhu, Z. Fan, Y. Wang, H. Zhang, W. Huang, T. Yu, Adv. Energy Mater. **5**, 1500559 (2015)
25. N.-Y. Wang, C.-H. Shih, P.-T. Chiueh, Y.-F. Huang, Energies **6**, 871–883 (2013)
26. Z.S.J. Liu, Y. Deng, Y. Zou, C. Li, X. Guo, L. Xiong, Y. Gao, F. Li, D. Zhao, Angew. Chem. **121**, 5989–5993 (2009)
27. W. Li, D. Zhao, Adv. Mater. **25**, 142–149 (2013)
28. M. Li, Y. Zhang, L. Yang, Y. Liu, J. Yao, Electrochim. Acta **166**, 310–319 (2015)
29. Y. Wu, Y. Li, L. Qin, F. Yang, D. Wu, J. Mater. Chem. B **1**, 204–212 (2013)
30. J. Liu, J. Xu, R. Che, H. Chen, M. Liu, Z. Liu, Chem. Eur. J. **19**, 6746–6752 (2013)
31. A.-L. Morel, S.I. Nikitenko, K. Gionnet, A. Wattiaux, J. Lai-Kee-Him, C. Labrugere, B. Chevalier, G. Deleris, C. Petibois, A. Brisson, M. Simonoff, ACS Nano **2**, 847–856 (2008)
32. P. Wang, M. Gao, H. Pan, J. Zhang, C. Liang, J. Wang, P. Zhou, Y. Liu, J. Power Sources **239**, 466–474 (2013)
33. X. Li, X. Huang, D. Liu, X. Wang, S. Song, L. Zhou, H. Zhang, J. Phys. Chem. C **115**, 21567–21573 (2011)
34. Z. Wang, D. Luan, S. Madhavi, Y. Hu, X.W. Lou, Energy Environ. Sci. **5**, 5252–5256 (2012)
35. X. Jia, Z. Chen, X. Cui, Y. Peng, X. Wang, G. Wang, F. Wei, Y. Lu, ACS Nano **6**, 9911–9919 (2012)
36. Z. Du, S. Zhang, J. Zhao, X. Wu, R. Lin, J. Nanosci. Nanotechnol. **13**, 3602–3605 (2013)
37. P. Poizot, S. Laruelle, S. Grugeon, L. Dupon, J.M. Tarascon, Nature **407**, 496–499 (2000)
38. B. Jin, A.-H. Liu, G.-Y. Liu, Z.-Z. Yang, X.-B. Zhong, X.-Z. Ma, M. Yang, H.-Y. Wang, Electrochim. Acta **90**, 426–432 (2013)
39. J. Luo, J. Liu, Z. Zeng, C.F. Ng, L. Ma, H. Zhang, J. Lin, Z. Shen, H.J. Fan, Nano Lett. **13**, 6136–6143 (2013)
40. Y. Wu, Y. Wei, J. Wang, K. Jiang, S. Fan, Nano Lett. **13**, 818–823 (2013)
41. G. Huang, S. Xu, S. Lu, L. Li, H. Sun, Electrochim. Acta **135**, 420–427 (2014)
42. Z. Zeng, H. Zhao, P. Lv, Z. Zhang, J. Wang, Q. Xia, J. Power Sources **274**, 1091–1099 (2015)
43. L. Su, Z. Zhou, M. Ren, Chem. Commun. **46**, 2590–2592 (2010)
44. L. Wang, W. Tang, Y. Jing, L. Su, Z. Zhou, ACS Appl. Mater. Interfaces **6**, 12346–12352 (2014)
45. J. Shin, H. Jung, Y. Kim, J. Kim, J. Alloys Compd. **589**, 322–329 (2014)